Combustion and Flame Multiplexed MHz-rate mid-infrared laser absorption spectroscopy for simultaneous in-chamber CO, CO_2 , H_2O, temperature, and pressure in a rotating detonation rocket engine

Nicholas Kuenning, Anil Nair, Alex Keller, Nicolas Minesi, Emre Ozen, Blaine Bigler, Jason Kriesel, John Bennewitz, Jason Burr, Stephen Danczyk, et al.

Available online at www.sciencedirect.com
ScienceDirect
Combustion and Flame 00 (2024) 1–21
Combustion and Flame

Multiplexed MHz-rate mid-infrared laser absorption spectroscopy for simultaneous in-chamber CO, CO_2, H_2O, temperature, and pressure in a rotating detonation rocket engine

Nicholas M. Kuenning[a,*], Anil P. Nair[a], Alex R. Keller[a], Nicolas Q. Minesi[a,b], Emre Ozen[c], Blaine Bigler[e], Jason Kriesel[c], John W. Bennewitz[1], Jason Burr[f], Stephen A. Danczyk[f], R. Mitchell Spearrin[a]

[a]*Department of Mechanical and Aerospace Engineering, University of California, Los Angeles (UCLA), CA 90095, USA*
[b]*Université Paris-Saclay, CNRS, CentraleSupélec, Laboratoire EM2C, 91190, Gif-sur-Yvette, France*
[c]*Opto-Knowledge Systems, Inc. (OKSI), Torrance, CA 90502, USA*
[d]*Jacobs Technology Inc., Edwards AFB, CA 93524, USA*
[e]*The University of Alabama in Huntsville, Hunstville, AL 35899, USA*
[f]*AFRL/RQRC, Combustion Devices Branch, Air Force Research Laboratory, Edwards Air Force Base, CA 93524, USA*

Abstract

A MHz-rate mid-infrared laser absorption sensing strategy has been developed to simultaneously measure the intra-cycle variation of carbon monoxide (CO), carbon dioxide (CO_2), water (H_2O), pressure, and temperature in the chamber of rotating detonating rocket engines (RDREs). The beams of two quantum cascade lasers (QCL) and one interband cascade laser (ICL) were multiplexed to target rovibrational transitions in the fundamental bands of CO and H_2O (at 5 μm) and CO_2 (at 4.2 μm). Extended trapezoidal injection current modulation via bias-tee circuitry provided sufficient spectral range to fully resolve collisionally broadened spectral transitions with a 1-μs time resolution. The three laser beams are coupled into a single optical fiber for light delivery though a sapphire window and into the annulus of a gaseous methane-oxygen rotating detonation rocket engine (RDRE) at the Air Force Research Lab in Edwards, CA. The light was retro-reflected from the annulus centerbody and spectrally demultiplexed onto two photovoltaic (PV) detectors. Quantitative, three-species concentration measurements along with temperature and pressure were inferred from the spectrally-resolved signals at 1 MHz over a range of post-detonation, in-chamber conditions, 1500–3000 K and 1–5 atm at targeted propellant mass flow rates ranging from 0.09–0.36 kg/s. The integrated five-parameter measurement scheme captures approximately 80% of the total combustion gas composition and fully characterizes the thermodynamic state at detonation-relevant time-scales, offering broad applicability to high-speed combustion flows.

Keywords: detonation, detonation-based propulsion, laser absorption spectroscopy, high bandwidth, rotating detonation engine, mid-infrared

*Corresponding author
Email address: kuenningn@ucla.edu (Nicholas M. Kuenning)

1. Novelty and Significance Statement

This work involves development and application of a novel five-parameter, sub-microsecond combustion diagnostic for highly dynamic gas properties in the chamber of a rotation detonation rocket engine. The laser spectroscopy method is uniquely comprehensive in defining thermodynamic state from simultaneous species (CO, CO_2, and H_2O), temperature, and pressure measurements attained using a multiplexed mid-infrared laser absorption strategy. The diagnostic captures 80-90% of the species composition, which reduces compositional uncertainty in collisional broadening and thereby provides for highly quantitative MHz-rate optical pressure measurement. The quantitative time-resolved pressure measurement is critical in the assessment of pressure-gain combustion systems, wherein traditional pressure transducers are largely inadequate, while the species and temperature measurements also serve as important reference data for simulations supporting the community efforts to advance rotating detonation engine technology.

2. Author Contributions

NMK: Data curation, Formal analysis, Investigation, Methodology, Software, Validation, Visualization, Writing – original draft, Writing – review & editing. APN: Conceptualization, Data curation, Formal analysis, Investigation, Methodology, Supervision, Writing – review & editing. ARK: Investigation. NQM: Data curation, Methodology, Supervision, Writing – review & editing. EO: Investigation. BB: Investigation, Methodology, Resources. JK: Funding acquisition, Project administration, Supervision. JWB: Conceptualization, Project administration, Writing – review & editing. JB: Investigation, Methodology, Resources, Supervision, Writing – review & editing. SAD: Investigation, Methodology, Resources, Supervision. RMS: Conceptualization, Funding acquisition, Investigation, Methodology, Project administration, Supervision, Validation, Writing – original draft, Writing – review & editing.

3. Introduction

In recent years, the performance increases of traditional deflagration-based rocket engines have plateaued and small increases in efficiency are associated with significant increases in system cost and complexity, prompting further research into detonation-based propulsion to further increase propulsion system efficiencies [1]. In theory, detonation-based (or pressure-gain) combustion achieves performance closely approximated by a constant-volume heat-release process, yielding lower entropy generation and higher thermal efficiencies than constant-pressure deflagration, which is the default heat-release mode of most state-of-the-art aerospace-relevant combustion devices [2]. Realizing these gains in a practical engine configuration has eluded engineers despite significant research effort; several engine architectures have been proposed, including pulse detonation engines and standing oblique detonation wave engines, however, none have reached a level of technical maturity to warrant widespread adoption [2, 3, 4, 5]. A promising detonation engine architecture is the rotating detonation rocket engine (RDRE) in which reactants are pressurized by the leading shock of a self-sustaining detonation wave propagating azimuthally around the combustion chamber. The self-pressurization of reactants in the combustion chamber theoretically enables a ∼10% increase in specific impulse for a given combustor inlet pressure when compared to a conventional rocket engine [6, 7]. Alternatively, the inlet pressure of the RDRE could be decreased while hitting an identical performance target as a constant-pressure device, reducing the mass of large pumps and high-pressure propellant tanks [8]. In addition to propellant feed system mass savings, increased post-reaction pressures behind the detonation wave result in a small propellant reaction zone, enabling complete combustion to be achieved in a shorter combustion chamber. Unfortunately, RDREs have proved challenging to design due to the uncertainty and dynamic nature of the detonation cycle, spanning a wide range of thermodynamic conditions at sub-millisecond time scales. The short time scales combined with extreme heat flux conditions in the chamber have also posed significant challenges to in-chamber diagnostics, exacerbating the challenge of understanding the root causes of gaps between theoretical performance and realized performance. As such, there exists a distinct need for high-bandwidth, in-chamber diagnostics that yield quantitative data which can provide more granular insights into the reacting gas dynamics of rotating detonation rocket engine operation.

Rotating detonation engine studies typically leverage traditional instrumentation such as load cells and pressure transducers. Average pressure and thrust measurement provide useful global performance metrics but lack the temporal and spatial resolution to probe intra-cycle variations which could contain useful information about combustion dynamics and specific loss mechanisms. High-bandwidth pressure transducers exist, offering responses in the 100's of kHz range; however, the harsh thermal environment requires these devices to be stood off from the chamber, complicating pressure measurement [9]. Non-intrusive optical diagnostics have proved highly valuable in detonation engine studies due to their high bandwidth and the capability to collect in situ data. High-speed videography positioned to view the injector head-on has been leveraged to visualize the number of detonation waves in the chamber and to measure detonation wave speeds. This data provides insight into the transient evolution of detonation wave structure but is integrated over the axial direction, spanning a wide range of thermochemical conditions thus complicating analysis [10]. Advances in optically accessible RDRE chamber outer bodies have enabled OH* chemiluminesence videography which captures the propagation of the detonation wave, providing qualitative assessments of wave propagation in the channel and subsequent heat release [11]. Other optical techniques applied to flows within RDREs are particle induced velocimetry (PIV) [12], coherent anti-Stokes Raman scattering (CARS) [13], and planar laser induced fluorescence (PLIF) [14]. Laser absorption spectroscopy (LAS) has proved to be a useful diagnostic method for RDRE studies, providing quantitative temperature, pressure, and species measurement in reacting flow environments with short time scales [15, 16]. Specifically, recent advances in temporal bandwidth to MHz rates has provided sufficient temporal resolution to resolve intra-cycle transients within RDREs with 5–20 kHz cycle frequencies [17, 18, 19, 20, 21, 16, 15, 22].

In this article we present a multiplixed mid-infrared laser absorption sensing strategy which enables simultaneous 1-MHz measurements of temperature, pressure, and three major combustion species (CO, H_2O, and CO_2) within the annulus of an RDRE. By capturing the intra-cycle evolution of these thermophysical properties, combustion progression and dynamics of the detonation flow field can be evaluated. This work advances upon our prior MHz-rate sensing strategies by simultaneously probing three distinct species mid-stream within the annular RDE chamber, while also improving the pressure and temperature measurement methods to reduce uncertainty at elevated pressures. The spectroscopic methods are implemented by developing a combined time- and wavelength-division multiplexing scheme to couple three mid-infrared lasers that share a single optical path through the engine. In Sec. 4 we overview the

fundamental theory and wavelength selection behind the mid-infrared laser absorption spectroscopy method and how thermophysical properties relate to the measured absorption spectra. Next, in Sec. 5 we detail the experimental setup on a methane-oxygen RDRE, detailing the opto-electronic design that enables MHz-rate, three-species measurement with the mid-infrared light sources. Section 6 discusses the improvements made to the spectroscopic data processing, including reduced uncertainty of the pressure measurement, and implementing a multi-line Boltzmann population fit to infer temperature. Using these data-processing methods, Sec. 7 shows how thermochemical properties are extracted from the measured absorption spectra at each time step and intra-cycle averaged properties are calculated.

4. Theoretical Approach

Laser absorption spectroscopy in the infrared domain may utilize rapidly-tunable semiconductor light sources to resolve spectral absorption features created by discrete rovibrational absorption transitions termed 'lines'. In this study we employ a scanned-wavelength direct absorption (scanned-DA) spectroscopic technique wherein the injection-current is modulated to rapidly tune the wavelength of the emitted laser light to resolve the lineshape of multiple spectral transitions within a 1-µs period. Rapid wavelength scanning enables correction of common convoluting factors such as beam steering and thermal emission, characteristic of harsh high-temperature environments [23]. Additionally, spectrally-scanned laser absorption is insensitive to line shifts from collisional effects and potential laser drift throughout the course of an experimental campaign. Figure 1 shows the targeted absorbance spectra at pressures representative of RDRE operation with the approximate spectral range captured by the lasers, showing the fully resolved features.

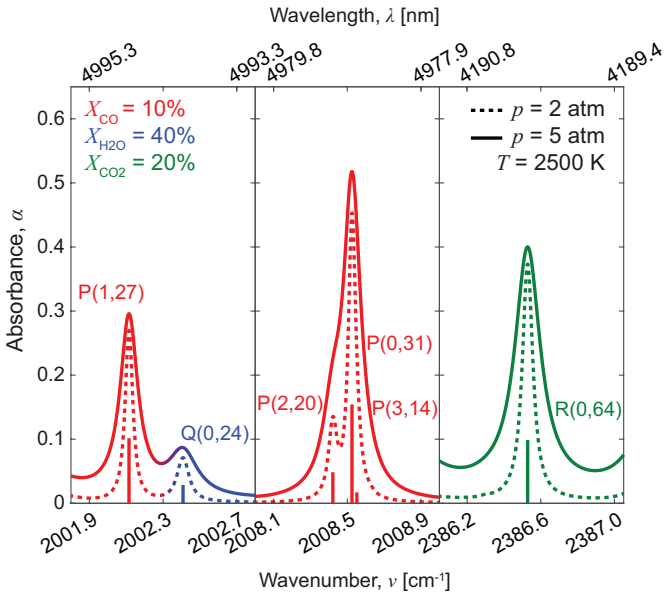

Figure 1. Simulated absorbance plots (using the HITEMP database [24]) of the three spectral ranges targeted in this study. The absorbance spectra are simulated at the expected thermochemical conditions within the annulus of the RDRE.

The light attenuated from spectral absorption during engine operation I_t and the background signal intensity before the test I_0 can be converted to an absorbance α using the relation $\alpha = -\ln(I_t/I_0)$. The absorption caused by each discrete rovibrational transition i of each species j is related to the thermophysical properties of the absorbing gas through the Beer-Lambert law, shown in Eq. 1. The Beer-Lambert law relates the measured absorbance spectra to the thermophysical properties of the flow: number density of species j, n_j [cm^{-3}], temperature, T [K], and pressure, P [atm], as well as the path length L [cm].

$$\alpha_{ij}(\nu) = -\ln\left(\frac{I_t}{I_0}\right) = n_j L S_{ij}(T)\phi_{ij}(\nu, P, T, X_Y) \tag{1}$$

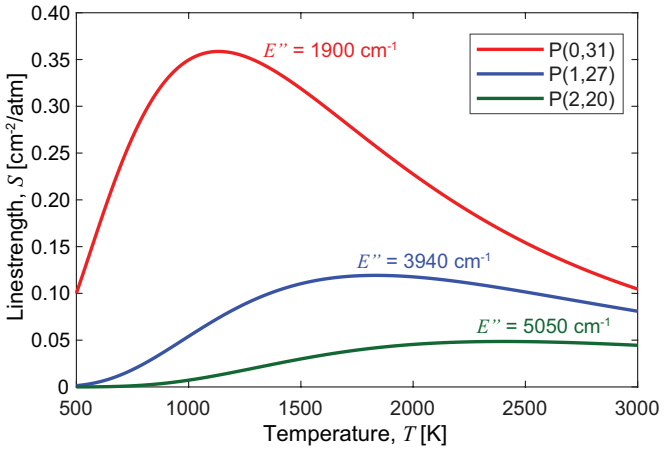

Figure 2. Linestrengths of the three CO transitions which are used to infer temperature.

The pressure and temperature dependence is contained within the linestrength S_{ij} [cm^{-1}/molecule·cm^{-2}] and lineshape ϕ_{ij} [cm^{-1}] functions. An additional dependence on flow composition X_Y is present within the lineshape function which requires additional treatment as discussed in Sec. 6. Equation 2 defines the temperature-dependent linestrength which relies on spectroscopic parameters including the partition function Q, lower-state energy E_j [cm^{-1}], and the center wavenumber of the transition $\nu_{0,j}$ [cm^{-1}], all documented in the HITRAN database [24].

$$S_j(T) = S_j(T_0)\frac{Q(T_0)}{Q(T)} \times \exp\left[-\frac{hcE''_j}{k}\left(\frac{1}{T}-\frac{1}{T_0}\right)\right] \times \left[1-\exp\left(-\frac{hc\nu_{0,j}}{kT}\right)\right] \times \left[1-\exp\left(-\frac{hc\nu_{0,j}}{kT_0}\right)\right]^{-1} \tag{2}$$

Detailed spectral line analysis is required to accurately infer temperature, pressure, and species abundance from measured spectra. Temperature can be calculated from the relative magnitude of line intensities (or state populations) which is primarily governed by the Boltzmann distribution and lower-state energy assignments of each line. Selecting transitions of disparate lower state energy can enable sensitive thermometry, but sufficiently measurable intensity over the targeted temperature range is also required. Typically, linestrengths providing an absorbance near 1 at the expected thermodynamic conditions produces the highest signal-to-noise ratio [25]. The lineshape function captures the effects of pressure via line broadening from collisions. Collisional broadening is 4–20x higher than Doppler broadening at the predicted conditions of the RDRE, making the broadening primarily Lorentzian, with a smaller Gaussian contribution from the Doppler effect [26]. The convoluted lineshape function, typically well-approximated by a Voigt profile, can be defined with knowledge of the collisional width $\Delta\nu_C$ and Doppler width $\Delta\nu_D$. In a collisionally dominated regime, such as that of an RDRE, the change in linewidth is linearly dependent on pressure, with additional dependence on temperature and gas composition as shown in Eq. 3.

$$\Delta\nu_C = P \times 2\gamma_{\mathrm{CO,mix}}(T, X_Y) \tag{3}$$

Specific methods for deconvoluting the effects of temperature and pressure on the absorbance spectra are discussed in Sec. 6.

Careful mid-infrared wavelength selection enables sensitive and robust detection of the target species. The fundamental vibrational bands of carbon monoxide (CO), water (H_2O, symmetric bending), and carbon dioxide (CO_2, asymmetric stretch)—centered near 4.7 µm, 6.3 µm, and 4.3 µm respectively—are orders of magnitude stronger (higher linestrength) than the overtone and combination bands in the near-infrared. Strong rovibrational absorption lines within these fundamental bands overlap in specific narrow spectral domains accessible with rapidly-tunable semiconductor light sources, providing the opportunity for high species sensitivity at short optical path lengths (~1 cm) such as those in the annuli of RDREs. The transitions targeted in this study were selected for their strength, temperature sensitivity, and spectral isolation from interfering absorption due to other combustion species at the conditions expected in the expanded detonation products of an RDRE (1000–4000 K and 1–5 atm).

Spectrally-resolved measurements of CO absorption were performed by targeting the P(0,31), P(1,27), and P(2,20) transitions in the fundamental vibrational bands (Δv=1) where P(v'',J'') indicates the respective lower vibrational (v'') and rotational (J'') quantum numbers. The P(1,27) line centered at 2002.11 cm^{-1} is shown in the left plot of Fig. 1 while the P(0,31) and P(2,20) lines, centered at 2008.53 cm^{-1} and 2008.42 cm^{-1} respectively, are shown in the center plot. By targeting transitions originating in the ground, first, and second vibrational states, the relative magnitudes of the absorbance transitions are sensitive to temperature over the range of relevant conditions (2000–3500 K). Figure 2 shows the temperature-dependent linestrength function of each of these transitions, illustrating the difference in temperature dependence of the three transitions. Previous works have targeted the P(0,31) and P(2,20) line pair [27, 28, 15]; however, Fig. 1 shows that these lines blend at elevated pressures which can complicate the interpretation of measured spectra. Adding the P(1,27) line as a third temperature sensitive CO transition enables a Boltzmann-fit temperature measurement scheme to be used as described in Sec. 6 [25], extending the range of conditions over which the method can be employed. The P(1,27) line was selected due to its temperature sensitivity complimenting the P(0,31) and P(2,20) transitions and its close proximity to a relatively strong water feature, enabling a two-species measurement with one light source.

The targeted H_2O feature near 5.0 μm, is a combination of two individual transitions of the ν_2 (symmetric bending) band, the $24_{0,24} \rightarrow 25_{1,25}$ and $24_{1,24} \rightarrow 25_{0,25}$ rovibrational doublet of the ν_2 fundamental band, where the notation $J_{K_a,\,K_b}$ refers to the rotational quantum number J and angular momentum K about the a and b axes. This line pair will be referred to as the "H_2O doublet" or Q(0,24) for the remainder of this work. This transition is centered at 2002.41 cm^{-1}, creating a favorable spacing of ~0.3 cm^{-1} from the P(1,27) CO line, allowing both transitions to be captured within the ~1 cm^{-1} tuning range of the laser but providing enough distance such that the lines do not blend significantly at elevated pressures. Carbon dioxide concentration measurements were performed by targeting the R(0,64) transition of the ν_3 asymmetric stretch band, centered near 2386.53 cm^{-1}.

5. Experimental Setup

All experiments were performed on a rotating detonation rocket test rig at the Air Force Research Laboratory in Edwards, CA. The RDRE test article was a standard design using gaseous CH_4 and O_2 as propellants and studied by several research groups focused on reproducing performance at independent test locations [1]. Measurements were made over approximately 1 s for a range of test conditions spanning mass flow rates of 0.09–0.36 kg/s at an equivalence ratio of 1.1. For each test, a maximum of 500 ms of raw intensity data was recorded, consisting of 50 ms before ignition, 100 ms of startup transient, and up to 350 ms of steady state data. The dataset duration was limited by the maximum memory available on the data acquisition system or, in some cases, window failure associated with thermo-mechanical stress. The shortest quasi-steady state test duration was ~50 ms, wherein the MHz measurement rate of the diagnostic provided ample data to assess gas properties (~50,000 scans or ~500 detonation cycles).

Two continuous-wave distributed-feedback (DFB) quantum cascade lasers (QCL) (ALPES Lasers), tunable from 2001 to 2012 cm^{-1}, were used as the narrow-band light sources for probing the CO and H_2O transitions while a third continuous-wave DFB interband cascade laser (ICL) (Nanoplus), tunable from 2382 to 2389 cm^{-1}, targeted the CO_2 transition. A bias-tee (SigaTek SB12D2D) configuration, detailed in Nair et al. [15] was used to bypass the bandwidth limitation of the commercial off-the-shelf laser controllers (Arroyo 6300 series), increasing the maximum achievable scan rate from 200 kHz to several MHz. Custom trapezoidal waveforms, scanning significantly below the lasing threshold, maximized tuning range during the 1-μs scan period using the bias-tee circuitry and a programmable function generator (Rigol DG1000Z) [29]. Supplied waveforms contained an 80-, 40- and 30-ns leading-edge ramp on the 4.99-μm, 4.98-μm, and 4.2-μm light sources respectively to prevent exceeding the detector bandwidth in the beginning portion of the scan. At 1 MHz, a scan depth of 0.74 cm^{-1} for the 4.99-μm light source, a scan depth of 0.96 cm^{-1} for the 4.98-μm light source, and a scan depth of 0.57 cm^{-1} for the 4.2 μm light source can be achieved, enabling targeted spectral features to be well-resolved at pressures up to approximately 5 atm.

Figure 3 illustrates the sensor hardware configuration and the interface with the engine. The multiplexed optical sensor consists of two optical breadboards: a 'remote' breadboard housing the three lasers connected (via optical fiber) to a 'detector' breadboard which pitches the light into the annulus and catches the retro-reflected light on two photovoltaic detectors. On the remote breadboard, the two QCL laser beams are combined using a 50/50 CaF_2 beamsplitter and further time-division-multiplexed by utilizing trapezoidal injection current waveforms with a duty cycle of 45% from a single function generator, enabling consistent phase-locking of the signals. A dichroic mirror

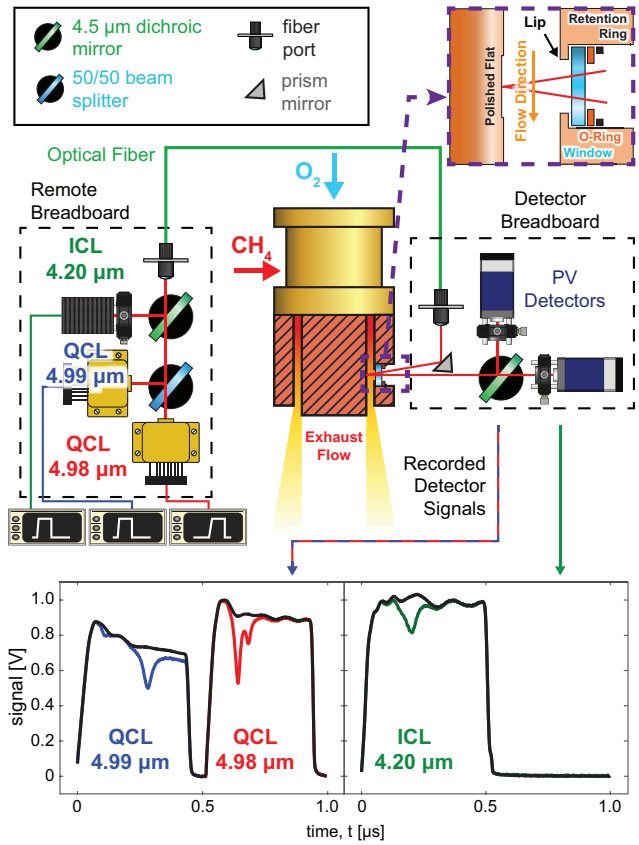

Figure 3. Optical hardware layout showing the optical access point on the RDRE chamber and retro-reflector (Top). Sample background (black) and transmitted signal (blue, red, and green) intensities recorded on the photovoltaic detectors (Bottom).

with a 4.5-µm cutoff transmits the 5µm light while reflecting the 4.2-µm light, making all three beams coincident with minimal loss of power. All three beams are pitched into a single fiber port, collimating the three beams into the InF_3 single-mode fiber. Combining the beams into a single fiber simplifies the delivery to the engine and keeps the breadboard closest to the engine as compact as possible. Light exits the fiber and is collimated to a ~1-mm diameter beam and pitched through a sapphire window into the annulus of the RDRE by adjusting a prism mirror. The top right sub-figure of Fig. 3 shows the exact configuration of the window and retro-reflector. A 12.7-mm diameter, 5-mm thick sapphire window is placed adjacent to the inner wall of the combustor outer body. The window is offset from the combustion gases by a thin metal lip and held in place with a retention ring threaded into the outer body. A silicone o-ring with a square-cross section is placed between the retention ring and window to reduce thermal-expansion induced stresses and minimize exhaust gas leakage across the window. The laser light is reflected off of a 6.3x6.3 mm flat milled onto the RDRE center body with a half angle of ~ 5°. After exiting the chamber, the light passes through another dichroic mirror with a cutoff at 4.5 µm, reflecting the 4.2-µm light and passing the 5-µm light onto two photovoltaic detectors (Vigo PVMI-4TE-8-1x1, 198-MHz bandwidth) with spectral bandpass filters at the respective light frequencies to reject broadband thermal emission. Sample laser intensities recorded by the PV detectors from the pre-test and test periods are shown in the bottom of Fig. 3. The time-division multiplexing scheme of the 5-µm light sources enables both intensities to be recorded on a single detector, saving significant cost and making the detector breadboard more compact. The relative wavenumber as a function of time is obtained by placing a germanium etalon in the beam path before a test and noting the time between successive constructive and destructive interference peaks of known wavenumber spacing (free spectral range).

6. Spectroscopic Data Processing

In this section we detail the specific data-processing steps used to extract thermophysical properties associated with the measured absorbance spectra. As mentioned in Sec. 4, the effects of temperature and pressure on molecular spectra are convoluted and must be separated to obtain accurate results. A particular sequence is utilized to accommodate the inter-dependence of gas properties. First, a line-fitting method is used to obtain the integrated absorption area and the line width of the target transitions. Once line areas are extracted, a Boltzmann population fit uses the measured CO line areas to infer temperature. After temperature is quantified, the pressure is inferred from the measured line widths of the CO spectra. Finally, once temperature and pressure are quantified, the species mole fractions are inferred via the Beer-Lambert law. These data-processing steps are applied to each measured laser scan, providing thermophysical properties as a function of time.

As discussed in Sec. 4, both the linestrength and lineshape functions are dependent on temperature; we seek to obtain the temperature as a function of linestrength only. A simplified expression of the Beer-Lambert law is obtained in Eq. 4 by integrating Eq. 1 and noting that $\int_{-\infty}^{\infty} \phi_{ij}(\nu)d\nu = 1$. Equation 4 shows the integrated absorbance area of transition i of species j, A_{ij} [cm^{-1}] is independent of the lineshape function ϕ.

$$A_{ij} = \int_{-\infty}^{\infty} \alpha_{ij}(\nu)d\nu = n_j L S_{ij}(T) \tag{4}$$

With this integration, the absorbance area is dependent on n, T, and linestrength S. Calculating the ratio of measured line areas eliminates the dependence on pathlength, number density, and pressure, yielding a measurement parameter than is primarily a function of temperature.

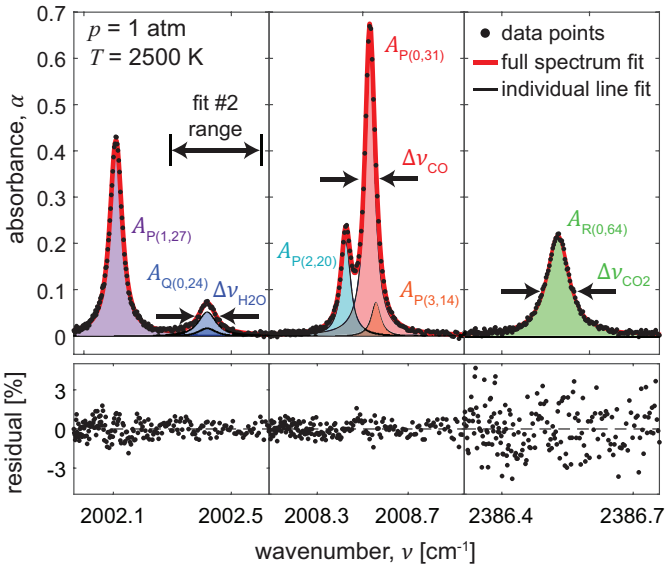

Figure 4. Measured absorbance spectra and resulting Voigt fit for a single 1-μs period of a $\dot{m}$ = 0.09 kg/s, ϕ = 1.1 test.

Spectral line areas and widths are extracted by minimizing the residual between the measured absorbance spectra and the sum of simulated Voigt profiles [30] approximating the shape of each line. Sample measured absorbance spectra, their corresponding Voigt fits, and their residual after fitting are shown in Fig. 4 for a single scan in the quasi-steady portion of a $\dot{m}$ = 0.09 kg/s, equivalence ratio ϕ=1.1 test. Rather than fitting all lines at once, a sequential three-part fitting routine is employed, with each part optimized to capture a different set of spectral properties. The key steps of this three-part routine are summarized in Fig. 5 and discussed in this section. Fit #1 prioritizes extracting CO line areas and widths of the P(0,31), P(1,27), and P(2,20) lines, from which the number density of CO n_{CO}, temperature T, and pressure p are calculated. While the Q(0,24) line is included in this initial fit, its lower magnitude compared to the P(1,27) line does not provide a reliable result. Fit #2 is performed between 2002.3–2002.6 cm^{-1},

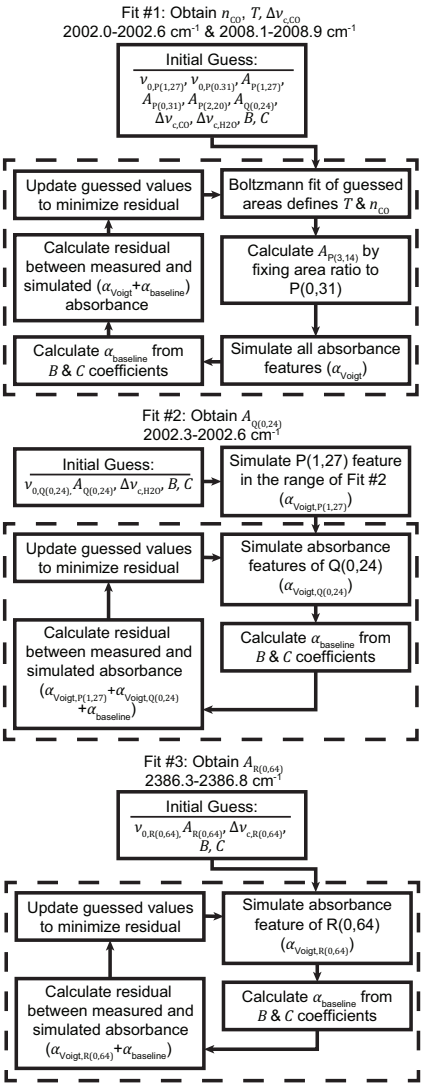

Figure 5. Voigt fitting procedure for the absorbance spectra measured at 4.98 µm and 4.99 µm. The steps within the least squares fitting routine are bounded by dashed boxes.

shown in Fig 4, fixing the CO line parameters and only floating the H_2O Q(0,24) doublet parameters to extract the area of the Q(0,24) doublet. A third fit (Fit #3) extracts the area of the CO_2 R(0,64) line.

The first fitting routine (Fit #1) extracts line areas, widths, and line positions from the light recorded at 4.99 µm and 4.98 µm, corresponding to the left two plots of Fig. 4. The Voigt lineshape approximation requires a line area A_i, collisional width $\Delta\nu_{c,i}$, Doppler width $\Delta\nu_{d,i}$, and line position $\nu_{0,i}$. Two factors complicating the fitting routine are the presence of the P(3,14) line centered at 2008.55 cm^{-1} and the insensitivity of the least squares fitting routine to trade offs between collisional and Doppler width, requiring one to be fixed in order to obtain an accurate result for the other. The flow will be collisionally dominated at the temperatures and pressures expected in the annulus of an RDRE ($\Delta\nu_{c,i} \sim$ 4–20x $\Delta\nu_{d,i}$), making the lineshape nearly Lorentzian. While the Doppler width is small, its contribution to the Voigt lineshape is non-negligible, requiring calculation at each time step. Additionally, the P(3,14) line area and width are unknown and it is difficult for the fit to accurately infer theses parameters, especially at higher pressures where the lines are blended. If not properly accounted for, this line can bias the area measurement of the P(0,31) line, biasing temperature measurement. Within the first routine, the P(0,31), P(1,27), and P(2,20) areas are fit which

defines a temperature, this temperature is then used to fix the area of the P(3,14) line and Doppler width of all lines. Details about the method used to convert line areas to a temperature are given in the next paragraph. Before fully accounting for the P(3,14) line, the collisional width must also be known. To simplify the fitting routine, all CO lines are assumed to have the same collision width. Nair et al. shows that this assumption introduces minimal error for the P(0,31), P(2,20), and P(3,14) lines at high-temperature combustion conditions [15]. We extend this assumption to the P(1,27) line, noting that the rotational quantum number J" = 27 is within the range of rotational quanta in the analysis by Nair et al. Finally, the line positions of all transitions are determined by floating the line positions of the P(1,27) and P(0,31) lines and fixing the line positions of the nearby lines for each spectral region respectively by noting the known relative line positions from the HITEMP database [24].

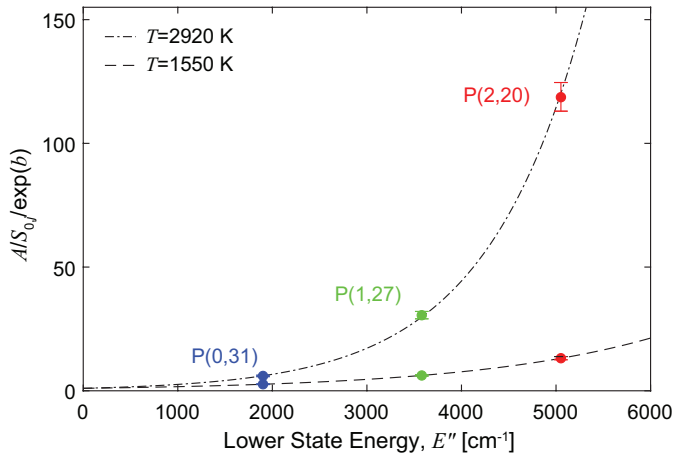

Figure 6. Measured areas normalized by reference linestrength and their respective Boltzmann population fit at two temperatures.

Temperature is inferred during the least squares minimization through a Boltzmann population fit. In LAS, the temperature is often inferred by utilizing the ratio of two transition areas [23, 31]. In a previous work [25], we developed a Boltzmann population fit method to account for more than two transitions to measure temperature and number density with reduced uncertainty. Equation 5 details how the ratio of integrated absorbance areas to the reference linestrength of transition i, $S^0_{i,\mathrm{CO}}$ [cm^{-1}/molecule·cm^{-2}], relates to n_{CO} and T, where E_i [cm^{-1}] is the lower-state energy of the transition [24], T_0 = 296 K and hc/k_B = 1.44 cm·K.

$$\ln\left(\frac{A_{i,\mathrm{CO}}}{S^0_{i,\mathrm{CO}}}\right) = \ln(Ln_{\mathrm{CO}}q(T)) - \frac{hc}{k_{\mathrm{B}}}\left(\frac{1}{T}-\frac{1}{T_0}\right)E_i \tag{5}$$

$q(T)$ represents the partition function taken from HITRAN [32, 33] multiplied by a stimulated emission factor, shown in Eq. 6 where ν_0 = 2005 cm^{-1} [25].

$$q(T) = \frac{Q(T_0)}{Q(T)}\frac{1-\exp\left(-\frac{hc}{k_{\mathrm{B}}T}\nu_0\right)}{1-\exp\left(-\frac{hc}{k_{\mathrm{B}}T_0}\nu_0\right)} \tag{6}$$

Writing Eq. 5 in the form of $Y = aE_i + b$ yields a slope and intercept, a and b, which are rearranged to solve for T and n_{CO} as shown in Eq.7 and Eq.8.

$$T = \frac{1}{1/T_0 - ak_{\mathrm{B}}/hc} \tag{7}$$

$$n_{\mathrm{CO}} = \frac{\exp(b)}{Lq(T)} \tag{8}$$

By utilizing the Boltzmann population fit, T is determined independently from other thermophysical properties and is considered a known for the subsequent fitting steps. Sample results of this Boltzmann population fit are shown in Fig 6. Note that in this figure the reference temperature has been set to T_0 = 1000 K to better illustrate the temperature sensitivity.

The last part of the fitting routine accounts for small variations in the measured signal intensity due to mechanical vibration, beam steering, broadband interference, and broadband emission. These effects can not be completely eliminated but are significantly reduced by thoroughly securing optical components, centering the beam on all optics, and utilizing spectral-bandpass filters. A key benefit of the MHz scanned direct absorption technique used is that these effects appear frozen on the time scale of an individual scan. Offsetting and scaling the background I_0 on a scan-by-scan basis as part of the fitting routine corrects for these effects to mitigate their influence on the measured properties and is captured by the B and C coefficients of Fig. 5. The guessed baseline coefficients are used to create a linear offset in the absorbance domain of the form $\alpha_{\text{baseline}} = B\nu + C$. These coefficients are floated in the fitting routine and correct for the effects of the harsh environment. The residual is then calculated between the measured absorbance and the sum of individual lines with the baseline correction. A least-squares fitting routine is employed to iterate on the guessed values until the residual reached a minimum value.

It should be noted that the residual of the aforementioned spectral fit is most sensitive to CO areas and temperature; however, the Q(0,24) line contributes relatively little to the total residual, making the fit less sensitive to the Q(0,24) line width and area. As such, after the routine displayed in Fig 5, a second fit (Fit #2) is performed between 2002.3–2002.6 cm^{-1}, fixing the temperature and CO parameters from the previous fit and floating only the Q(0,24) line area and collisional width. This second fit significantly decreases variation in the H_2O line areas that are an artifact of the insensitivity of the previous fit. A third fitting routine (Fit #3) is performed on the CO_2 line, floating the CO_2 line position, area, and collision width. The results of all fitting routines are shown in Fig. 4. Notably, the residuals are typically <3% for the CO features and <5% for the CO_2 features. Residuals plotted in Fig. 4 are normalized by the peak absorbance value within their respective spectral domains; the Q(0,24) line fit residual is typically <10% when normalized by the peak absorbance between 2002.3–2002.6 cm^{-1}. The measured line widths and areas are then converted to a pressure and mole fraction measurements.

Pressure P [atm] is determined by utilizing Eq. 3 with the measured collisional linewidths $\Delta\nu_C$ [cm^{-1}] and estimated collisional-broadening coefficient $\gamma_{\text{CO,mix}}$ [cm^{-1}/atm]. Collisional linewidth is dependent on the rate of collisions of the absorbing species with itself and other species in the reacting flow, making it linearly dependent on pressure. Each collision partner contributes to the aggregate collisional broadening coefficient of the mixture, characterized by the collisional broadening coefficient of each species $\gamma_{\text{CO},j}$ [cm^{-1}/atm]. These species-specific collisional broadening coefficients effectively represent the incremental collisional width per partial pressure of species j. The total collisional-broadening coefficient is obtained by taking a mole-fraction-weighted sum of the individual species' broadening coefficients as shown in Eq. 9.

$$\gamma_{\text{CO,mix}}(T, X_Y) = \sum_j X_j \gamma_{\text{CO},j} \tag{9}$$

Accurate determination of $\gamma_{\text{CO,mix}}$ often proves difficult due to a lack of reference broadening coefficients for many combustion species. Nair et al. [26] provide a method for simplifying this calculation for CO by considering only combustion species with $X_j > 1\%$ and documents the necessary reference coefficients to calculate $\gamma_{\text{CO,mix}}$ for CH_4–O_2 combustion. While the major combustion products have documented broadening coefficients with CO, many minor species and intermediates remain unmeasured due to difficulty in forming them in appreciable quantities to make an accurate measurement of the broadening coefficient. These remaining species must have their broadening coefficients estimated by leveraging scaling arguments based on the dependence of collision rate on the reduced mass and collision diameter of each species. The balance gas concentrations are estimated by simulating the combustion conditions with thermochemical models. Here, the GRI-MECH 3.0 [34] is paired with the CalTech Shock and Detonation Toolbox [35] in Cantera [36] to approximate the gas composition immediately behind the detonation wave (frozen composition) and when the flow is chemically equilibrated after being isentropically expanded from the CJ condition. These two states represent the thermodynamic extremes of flow composition for a given equivalence ratio ϕ. Evaluating $\gamma_{\text{CO,mix}}$ at the frozen and equilibrated conditions shows < 5% variation between the two conditions. Test in which H_2O and CO_2 data were available enabled a further reduction of uncertainty because a majority ($\gtrsim$ 80%) of species were measured, further constraining the broadening model. The remaining ~ 20% of species are estimated by initializing a gas in Cantera and balancing the concentrations of hydrogen, and oxygen at each time such that the entire mixture (including measured species) matched the targeted equivalence ratio of the test. This Cantera gas is equilibrated at the measured temperature and pressure of each time, approximating the remaining non-measured species.

When the broadening model is constrained to the measured species the pressure uncertainty is dominated by the uncertainty introduced in the reference broadening coefficient $\gamma_{CO,mix}$ from the measured mole fraction uncertainties. The uncertainty in pressure when assuming concentrations bound between the frozen and equilibrium conditions is 6%, incorporating the CO, H_2O, and CO_2 measurements into the broadening model reduces the uncertainty to 5% as reported in Appendix A. Additionally, Fig 8 shows that H_2O and CO_2 data are typically bounded between the frozen and equilibrium conditions, further justifying this approximation in cases where H_2O and CO_2 data are not available. This estimation of $\gamma_{CO,mix}$ enables a pressure to be quantitatively inferred from each measured collision width.

With temperature determined n_{H_2O} and n_{CO_2} [cm^{-3}] are found using Eq. 10. The CO number density n_{CO} is already known from the first fitting routine and Eq. 8.

$$n_i = \frac{A_i}{S_i(T)L} \tag{10}$$

The total number density, n_{tot}, is calculated with $p = n_{tot}k_bT$. The species mole fractions are then deduced with n_i/n_{tot}. The species mole fraction is a useful metric because it removes the variation in number density due to pressure, providing more detail about the chemical reactions occurring in the cycle. It should be noted that CO, H_2O, and CO_2 typically account for more than 80% of the product gas composition for fuel-rich CH_4–O_2 combustion.

7. Results

Experimental data was recorded for mass flow rates between $\dot{m}$ = 0.09–0.36 kg/s and an equivalence ratio of ϕ=1.1. In this section, we highlight key steps and results in converting the time-resolved spectral properties of CO, H_2O, and CO_2 into time-resolved and cycle-averaged measurements of temperature, pressure, and species mole fraction on an example test of $\dot{m}$ = 0.09 kg/s and ϕ = 1.1.

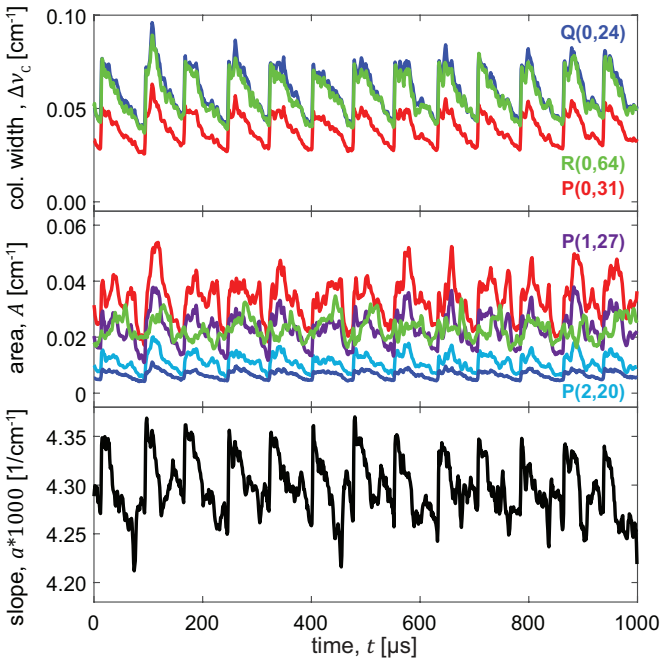

Figure 7. Line properties extracted from the Voigt fitting routine over a 1000-μs period of quasi-steady RDRE operation at $\dot{m}$ = 0.09 kg/s, ϕ = 1.1

After performing the Voigt fitting procedure described in Sec. 6, both the spectral line areas and collision widths are known as a function of time. The top and middle plots of Fig. 7 show the evolution of the collision widths and areas of the targeted features over a 1000 μs period of quasi-steady state RDRE operation. Both collision widths and areas follow a clear cyclic variation with a period on the order of 75 μs, approximately the expected period of detonation waves moving at a wavespeed of ~ 1.5 km/s [22]. As the detonation wave consumes propellant, a discontinuity

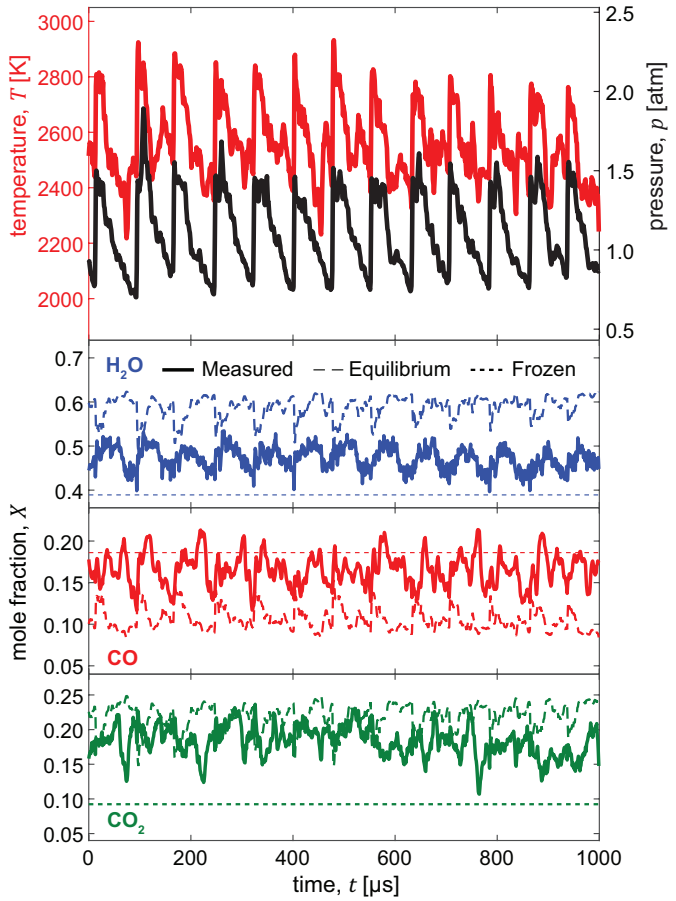

Figure 8. Inferred thermochemical properties extracted from the line properties plotted in Fig. 7.

is formed between the high post-detonation pressure and lower pressure of expanded reactants. This pressure discontinuity forms an oblique shock wave which is the primary driver of the pressure trends at the measurement location [22]. The collisional width is most strongly correlated with pressure, explaining the strong rise as the oblique shock wave passes, followed by an expansion. Both the H_2O and CO_2 lines exhibit larger collisional widths than the CO lines due to their larger collisional cross-section, i.e. larger molecules collide more frequently with the surrounding gas molecules (higher γ), increasing collisional broadening. Line areas exhibit a clear cyclic trend as well, though distinct from that of the collision widths, reflecting the additional species and temperature dependence. Following the Boltzmann fitting procedure of Sec. 6, the natural logarithm of the ratio of each CO line area and its reference line strength is fit as a function of lower state energy, resulting in a slope a that is a strong function of temperature. The bottom plot of Fig. 7 shows the variation of this slope with time. Sharp increases in this slope are strongly correlated with collision width increases, indicating the increase of both temperature and pressure across the oblique shock. As outlined in Sec. 6, the Boltzmann slope is converted into a temperature, the CO line widths are converted into a pressure, and the line areas of all species are converted into species mole fractions.

The results of this conversion are plotted in Fig. 8 for the same test time period as the line properties in Fig. 7. Similar to the collision widths of Fig. 7, the pressure trace of Fig. 8 exhibits a clear cycle beginning with the passage of the oblique shock followed by a nearly monotonic decrease in pressure until the next cycle begins. The temperature follows a similar cyclic trend, however, the temperature trend after the oblique shock is not monotonic—rather there is typically a sharp decrease, followed by a slight rise near the region immediately before the next wave. This non-monotonic trend is best seen near 450 μs where there is a ~400 K increase in temperature near the end of the cycle, which then decreases by ~200 K before the arrival of the next oblique shock. Since the pressure is decreasing during

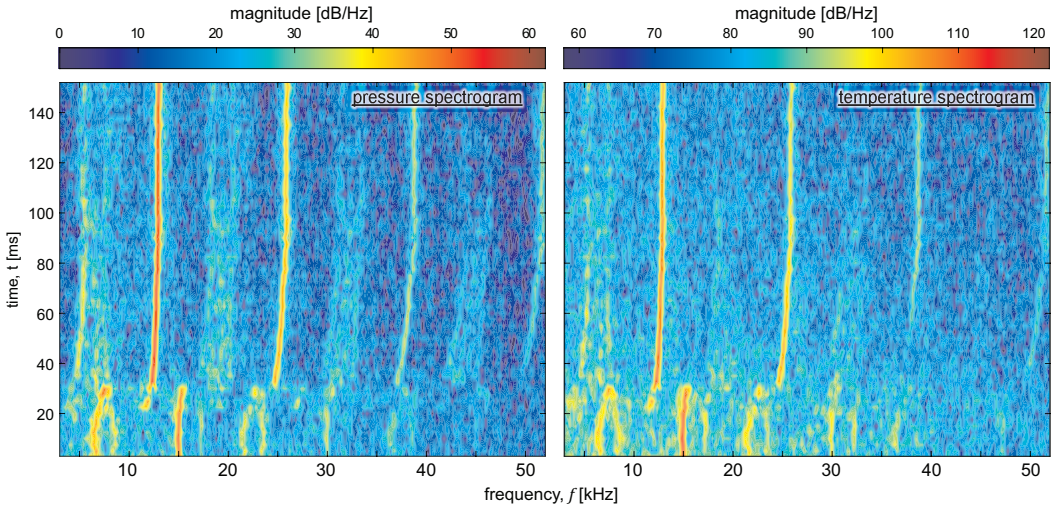

Figure 9. Short-time Fourier transform of the measured pressure (Left) and temperature (Right) over the period of engine operation of a $\dot{m}$ = 0.09 kg/s, ϕ = 1.1 test.

this entire period, this temperature variation is not a product of expansion or compression, but rather an indication that the gas has undergone a different thermochemical process upstream. These trends will become more apparent when cycle-averaged properties are examined.

The scale of cycle-to-cycle variation confirms the need for high-speed diagnostics to resolve intra-cycle properties as opposed to bulk averaged measurements. Plots of mole fraction in the bottom part of Fig. 8 display significant variation with time. Water mole fraction establishes a cyclic trend in which the mole fraction is near 0.45 at the beginning of the cycle, increases to ∼0.5 near the middle of the cycle before returning to ∼0.45 at the end of the cycle. The cycle-to-cycle trends of CO and CO_2 are more complex and not every cycle exhibits similar behavior. Overall, CO typically begins the cycle at a lower value, near 0.15 and increases to ∼0.2 near the middle of the cycle. Mole fractions serve as a useful quantity opposed to number density or partial pressure because it removes the influence of the pressure variation of the flow on markers of species concentration. The cyclic trends of mole fraction seem to lag the pressure and temperature rise associated with the oblique shock passage, which is suggestive of the shifting chemical equilibrium composition as the thermodynamic conditions (P, T) of the gas vary throughout the cycle. The mole fractions predicted for post-detonation composition ("frozen") and for local chemical equilibrium ("equilibrium") are plotted as dashed lines in Fig. 8. Frozen and equilibrium calculations are performed using GRI-MECH 3.0 [34] in Cantera [36] with the CalTech Shock and Detonation Toolbox [35]. Frozen results are obtained by calculating the post-detonation composition of a mixture of methane and oxygen at ϕ = 1.1 with an initial pressure given by the average pressure recorded by pressure transducers at the injector face. Equilibrium values are obtained by initializing a gas object at the predicted equivalence ratio of the test, in this case ϕ = 1.1, and equilibrating it at the measured temperature and pressure at each time. The measured water mole fraction is consistently between the equilibrium and frozen values and tends to be closer to the equilibrium value immediately following the passage of the oblique shock. Thermochemical equilibrium calculations predict a rise in water mole fraction with decreasing temperature, a trend which is observed in the data near the middle of the cycle, but does not predict the drop in water mole fraction observed near the end of the cycle. This drop near the end of the cycle is indicative that gas near the end of the cycle is further from thermochemical equilibrium than at the beginning of the cycle. Similar to water mole fraction, CO and CO_2 tend to be near the predicted equilibrium values near the beginning of the cycle. Mathews et al. [16] observed a similar trend of CO concentration data being closest to thermochemical equilibrium near the beginning of the cycle. Near the middle of the cycle, CO mole fraction tends to be above the predicted frozen value. Previous works have observed a trend showing rising CO concentrations in the middle of the cycle, attributed to a local variation in equivalence ratio due to asymmetric injector dynamics, pushing the propellant mixture temporarily to a more fuel-rich condition [15].

Cycle-to-cycle variation can be assessed in a more quantitative way by partitioning the data into individual cycles

and comparing the variation of each cycle to the average. The procedure for determining these cycle ensemble statistics is given in [22], but the main steps are summarized here. First, a short-time Fourier transform (STFT) is performed on the pressure and temperature data with a 5 ms data interval and a 0.25 ms overlap using a Hamming window. The short-time Fourier transform of pressure and temperature are shown in Fig. 9 for a representative test. Time zero in Fig. 9 corresponds to the drop in measured signal intensity from the passage of the driving detonation wave from the pre-detonator. For this test, a ~30 ms startup transient is observed marked by no clear dominant frequency in the power spectrum. After ~30 ms, the dominant frequency in the power spectrum occurs near 13 kHz, corresponding to the approximate cycle frequency observed in the time-resolved results. As time progresses from 30 ms to 70 ms, the dominant 13 kHz frequency slightly increases in frequency until stabilizing at 70 ms, past this point the engine has entered quasi-steady operation. Within the quasi-steady phase, each cycle is found by searching for the sharp increase in pressure observed across the oblique shock, i.e. by locating the local maxima of $\Delta P/\Delta t$ within the period of time determined by the peak frequency of the STFT. After identifying the bounds of individual cycles, we aggregate all cycles within the steady-state portion of the test to construct the average intra-cycle ensemble profiles and statistical variations. Figure 11 shows the intra-cycle ensemble pressure, temperature, and CO mole fraction for the 0.09 kg/s case in blue.

A similar procedure is applied to higher flow rate tests as well to yield time-resolved temperature, pressure, and species. A sample fit absorbance spectra from the 0.36 kg/s test case is shown in Fig. 10. As expected, at higher pressures the spectra has broadened significantly to the point where lines which were previously isolated now overlap, particularly the P(0,31) and P(2,20) are almost completely blended. In these cases the addition of the P(1,27) line adds significant benefit to the fitting routine since it remains better isolated than the lines near 2008 cm^{-1}, allowing for accurate recovery of temperature at extended pressures.

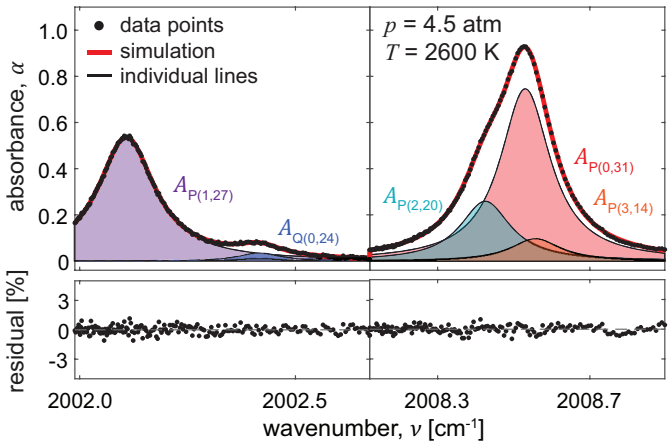

Figure 10. Measured absorbance spectra and resulting voigt fit for a single 1-μs period of a $\dot{m}$ = 0.36 kg/s, ϕ = 1.1 test.

The top two plots of Fig 11 show the intra-cycle ensemble profiles of pressure and temperature at different propellant flow rates. The solid lines indicate the average properties over the quasi-steady period while the transparent swaths represent the bounds of the 90th percentile of data, indicating the variation of the properties observed. The measured pressures increase with mass flow rate as expected, with intra-cycle trends that are similar. Flow rates below 0.36 kg/s have a brief plateau followed by a monotonic decrease, while the pressure of the 0.36 kg/s exhibits a slight rise after the oblique shock followed by a monotonic decrease. As observed in the time-resolved data, the temperature trend exhibits a rise across the oblique shock followed by a decrease to a local minimum before another slight rise followed again by a decrease to a minimum. The dip in temperature across all three tests is correlated with a rise in CO concentration shown in the bottom of Fig 11. Previous works have measured a similar intra-cycle drop and recovery in temperature correlating to a rise in CO concentration [15]. This trend is attributed to a locally fuel-rich condition causing a rise in carbon monoxide and a drop in combustion temperature. As the detonation wave passes the injector, the high post-detonation pressures can slow/ halt propellant injection. The fuel and oxidizer injector elements may not reestablish flow simultaneously, creating a locally off-nominal mixture ratio. In this case the middle of the cycle

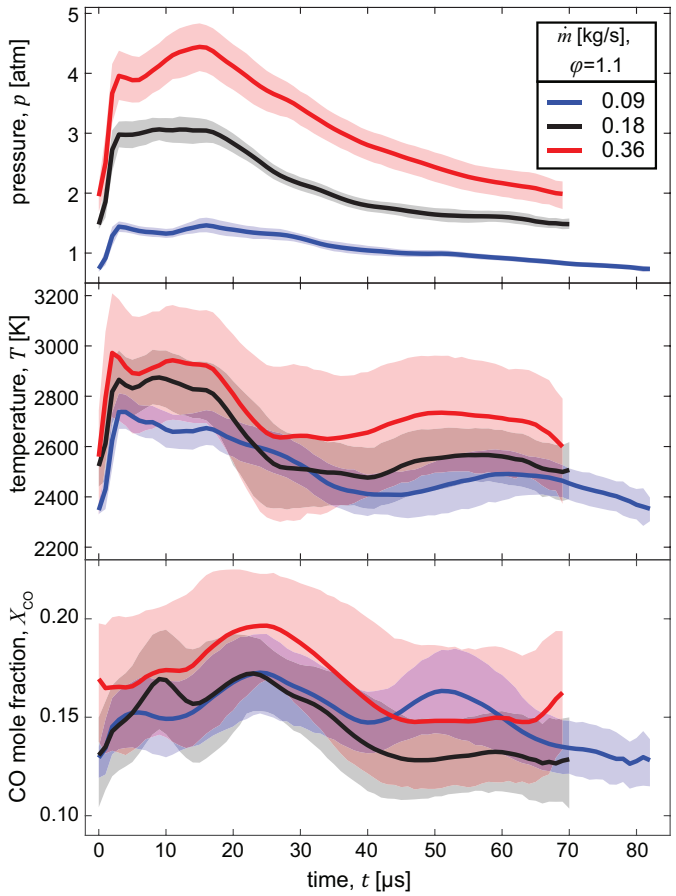

Figure 11. Intra-cycle ensemble averaged thermochemical properties over the quasi-steady engine operation period established by Fig. 9. Transparent swaths denote the range between the 10th and 90th percentile of the data.

tends to be more fuel rich. The measurement of such intra-cycle variations highlights the benefit of MHz-rate laser diagnostics for RDE development.

8. Conclusions

A MHz rate mid-infrared laser absorption sensing strategy for simultaneous measurements of carbon monoxide (CO), carbon dioxide (CO_2), and water (H_2O) has been developed and deployed inside the annulus of a rotating detonation rocket engine. This time- and wavelength-multiplexed sensor has been demonstrated to capture approximately 80% of the product gas composition of a methane-oxygen RDRE, thoroughly defining its thermochemical state at microsecond time-resolution. The time-division multiplexing scheme was employed to enable a 2-species, temperature, and pressure measurement on a single photovoltaic detector in a one microsecond time interval. A Boltzmann fitting strategy involving three distinct CO absorption transitions reduces temperature uncertainty at higher pressures. The comprehensive speciation measurements reduce compositional uncertainty, which in turn reduces pressure measurement uncertainty from collisional broadening. In-chamber measurements were performed on a methane-oxygen RDRE, providing data at pressures between 2–5 atm for a range of mass flow rates in the range 0.09–0.36 kg/s. Time-resolved MHz data provides insights regarding intra-cycle variation and start-up behavior of the RDRE. Intra-cycle ensemble averaged data was extracted and facilitated a comparison between the average properties of different test conditions. This multi-parameter spectroscopic measurement technique offers broad applicability to high-speed propulsion flows. Future work will consist of further extending the spectral measurement range to target absorbance transitions at higher pressures, enabling measurements near the injector plane of an RDRE.

Acknowledgements

This work was supported by the Air Force Research Laboratory (AFRL) and OptoKnowledge Systems Inc. under a Small Business Technology Transfer (STTR) program, Award No. FA864920C0326 with Dr. Eric Paulson as contract monitor, and Dr. Jason Kriesel as collaborator. Supplementary support was provided by the U.S. National Science Foundation (NSF), Award No. 1752516 and the Air Force Office of Scientific Research (AFOSR) Young Investigator Program (YIP) Award No. FA9550-19-1-0062 with Dr. Chiping Li as Program Officer. Distribution Statement A: Approved for public release. Distribution is unlimited. PA# AFRL-2024-2469. The authors would also like to thank Isaiah Jaramillo for assistance in running RDRE tests and Ilya Dunayevskiy for assistance in procuring hardware.

Appendix A. Uncertainty analysis

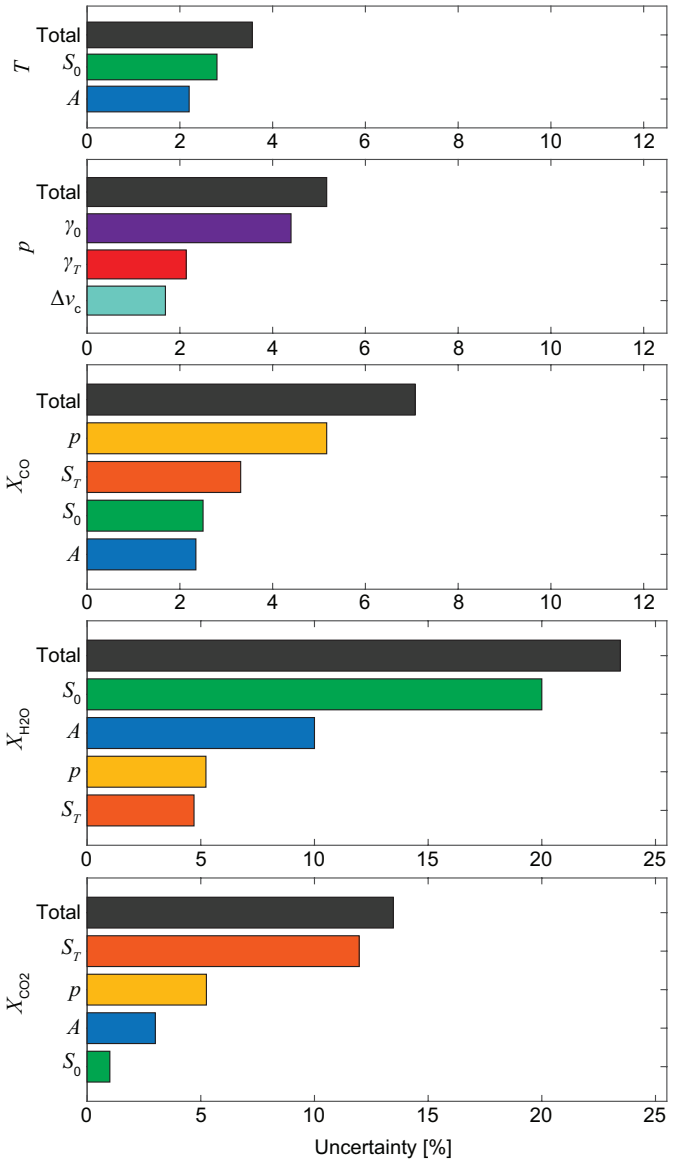

Figure A.12. Representative uncertainties for the temperature T, pressure p, and mole fractions of CO X_{CO}, H_2O $X_{\mathrm{H_2O}}$, and CO_2 $X_{\mathrm{CO_2}}$

In this section we estimate the uncertainties in the inferred thermochemical properties. Other works have outlined detailed uncertainty analyses which we will follow here, highlighting key steps for clarity [15, 16, 26, 25].

Since all thermochemical properties have a temperature dependence, we begin by estimating the uncertainty from the Boltzmann population fit. The temperature uncertainty primarily stems from uncertainty in the three CO line areas A and uncertainty in the reference line-strength listed in HITEMP S_0. Symbols listed in the text will correspond to the labels of uncertainty sources in Fig. A.12. As outlined by Nair et al. [15], the uncertainty in area accounts for uncertainty from the fit residual, the assumption that all CO lines have the same line width, and the listed linestrength uncertainty of the P(3,14) line. A linear fitting routine accounting for uncertainties is outlined by York et al. [37] and is used here to calculate the uncertainty in Boltzmann fit slope from the uncertainties in area and reference line strength.

Next, the pressure uncertainty is determined by accounting for the uncertainty in broadening coefficient and in the measured linewidth. Broadening coefficient uncertainty is assessed by accounting for the variation in broadening coefficient γ_0 between different flow compositions within the range of the uncertainty of the measured species and temperatures within the previously calculated temperature uncertainty γ_T [15, 26]. The assumption that all CO lines have the same linewidth, the linestrength uncertainty of the P(3,14) line and the calculated 1-σ uncertainty of the measured collision widths are added in quadrature to arrive at the collisional width uncertainty.

Species mole fraction uncertainties are obtained by combining uncertainty in reference linestrength and area (discussed previously) with the uncertainties in temperature dependent linestrength and pressure. The previously obtained uncertainty in temperature is propagated to the linestrength calculation to obtain the temperature dependent linestrength uncertainty. Adding these uncertainties yields mole-fraction uncertainties for each species. CO has the lowest combined uncertainty due to its strong absorption features and low database uncertainty, leaving the total uncertainty to be dominated by uncertainty in pressure. The mole-fraction uncertainty of CO in this work is higher than the 'column density' reported in previous works [15] due to the dependence on the pressure measurement uncertainty. The number density of CO has an uncertainty of 4.5% because its uncertainty is independent of pressure and dominated by line-strength uncertainty, which is significantly lower, as is seen in Fig. A.12. H_2O has the highest combined uncertainty due to a high reference-linestrength uncertainty. It is important to note that this reference-linestrength uncertainty will apply a bias to the data but does not affect the relative trends in the data. Beyond the database uncertainty, H_2O mole-fraction uncertainty is dominated by fit uncertainty due to the relatively weak feature. CO_2 has low reference-linestrength uncertainty and a low residual, having an uncertainty dominated by the uncertainty in temperature-dependent linestrength. The relatively low lower-state energy means this line has a relatively high $\partial S/\partial T$, making the relatively small uncertainty in temperature have a large impact on the linestrength. Future works should utilize a CO_2 line with a higher lower-state energy.

References

[1] J. W. Bennewitz, J. R. Burr, B. R. Bigler, R. F. Burke, A. Lemcherfi, T. Mundt, T. Rezzag, E. W. Plaehn, J. Sosa, I. V. Walters, S. A. Schumaker, K. A. Ahmed, C. D. Slabaugh, C. Knowlen, W. A. Hargus, Experimental validation of rotating detonation for rocket propulsion, Sci. Rep. 13 (2023) 14204.

[2] K. Kailasanath, Applications of detonations to propulsion - A review, in: 37th Aerospace Sciences Meeting and Exhibit, 1999, p. 1067.

[3] P. Wolański, Detonative Propulsion, Proc. Comb. Inst. 34 (2013) 125–158.

[4] W. H. Heiser, D. T. Pratt, Thermodynamic Cycle Analysis of Pulse Detonation Engines, J. Propul. Power 18 (2002) 68–76.

[5] S. A. Ashford, G. Emanuel, Oblique detonation wave engine performance prediction, J. Propul. Power 12 (1996) 322–327.

[6] B. R. Bigler, E. J. Paulson, W. A. Hargus, Idealized Efficiency Calculations for Rotating Detonation Engine Rocket Applications, in: 53rd AIAA/SAE/ASEE Joint Propulsion Conference, 2017, p. 5011.

[7] B. A. Rankin, M. L. Fotia, A. G. Naples, C. A. Stevens, J. L. Hoke, T. A. Kaemming, S. W. Theuerkauf, F. R. Schauer, Overview of performance, application, and analysis of rotating detonation engine technologies, J. Propul. Power 33 (2017) 131–143.

[8] J. Bradford, S. Bornstein, H. Magill, Performance and Business Case Impact Assessment for Launch Systems Utilizing RDRE Propulsion, in: 2022 IEEE Aerospace Conference (AERO), 2022, pp. 1–12.

[9] R. Gejji, I. Walters, S. Beard, A. Lemcherfi, S. Sardeshmukh, S. Heister, C. Slabaugh, Transducer installation effects on pressure measurements in pressure gain combustion devices, in: AIAA Aerospace Sciences Meeting, 2018, 2018, p. 0158.

[10] J. R. Burr, E. Paulson, Thermodynamic Performance Results for Rotating Detonation Rocket Engine with Distributed Heat Addition using Cantera, in: AIAA Propulsion and Energy 2021 Forum, 2021, p. 3682.

[11] R. B. Wang, A. M. Webb, R. Camacho, M. N. Slipchenko, J. Braun, T. R. Meyer, V. Athmanathan, C. Fugger, S. Roy, High-speed Chemiluminscence and OH-PLIF Imaging for Characterization of Reactant Refill and Detonation Wave Dynamics in a CH4-GOx RDRE., in: AIAA SCITECH 2024 Forum, 2024, p. 1032.

[12] D. Depperschmidt, R. Miller, J. Tobias, M. Uddi, A. K. Agrawal, J. B. Stout, Time-Resolved PIV Diagnostics to Measure Flow Field Exiting Methane-Fueled Rotating Detonation Combustor, in: AIAA Scitech 2019 Forum, 2019, p. 1514.

[13] V. Athmanathan, K. A. Rahman, D. K. Lauriola, J. Braun, G. Paniagua, M. N. Slipchenko, S. Roy, T. R. Meyer, Femtosecond/picosecond rotational coherent anti-Stokes Raman scattering thermometry in the exhaust of a rotating detonation combustor, Combus. Flame 231 (2021) 111504.

[14] B. A. Rankin, C. A. Fugger, D. R. Richardson, K. Y. Cho, J. L. Hoke, A. W. Caswell, J. R. Gord, F. R. Schauer, Evaluation of mixing processes in a non-premixed rotating detonation engine using acetone PLIF imaging, in: 54th AIAA Aerospace Sciences Meeting, Vol. 0, 2016, p. 1198.

[15] A. Nair, D. Lee, D. Pineda, J. Kriesel, W. Hargus, J. Bennewitz, S. Danczyk, R. Spearrin, MHz laser absorption spectroscopy via diplexed RF modulation for pressure, temperature, and species in rotating detonation rocket flows, Appl. Phys. B-Lasers O 126 (2020) 138.

[16] G. C. Mathews, M. G. Blaisdell, A. I. Lemcherfi, C. D. Slabaugh, C. S. Goldenstein, Aaron, I. Lemcherfi, Carson, D. Slabaugh, Christopher, S. Goldenstein, High-bandwidth absorption-spectroscopy measurements of temperature, pressure, CO, and H 2 O in the annulus of a rotating detonation rocket engine, Appl. Phys. B-Lasers O 127 (2021) 1–23.

[17] W. Y. Peng, S. J. Cassady, C. L. Strand, C. S. Goldenstein, R. M. Spearrin, C. M. Brophy, J. B. Jeffries, R. K. Hanson, Single-ended mid-infrared laser-absorption sensor for time-resolved measurements of water concentration and temperature within the annulus of a rotating detonation engine, Proc. Combust. Instit. 37 (2019) 1435–1443.

[18] C. S. Goldenstein, R. M. Spearrin, J. B. Jeffries, R. K. Hanson, Infrared laser absorption sensors for multiple performance parameters in a detonation combustor, Proc. Combust. Instit. 35 (2015) 3739–3747.

[19] R. M. Spearrin, C. S. Goldenstein, J. B. Jeffries, R. K. Hanson, Quantum cascade laser absorption sensor for carbon monoxide in high-pressure gases using wavelength modulation spectroscopy, Appl. Optics 53 (2014) 1938, iSBN: 1559-128X.

[20] S. T. Sanders, J. A. Baldwin, T. P. Jenkins, D. S. Baer, R. K. Hanson, Diode-laser sensor for monitoring multiple combustion parameters in pulse detonation engines, Proc. Combust. Instit. 28 (2000) 587–594.

[21] A. W. Caswell, S. Roy, X. An, S. T. Sanders, F. R. Schauer, J. R. Gord, Measurements of multiple gas parameters in a pulsed-detonation combustor using timedivision-multiplexed Fourier-domain mode-locked lasers, Appl. Optics 52 (2013) 2893–2904.

[22] A. P. Nair, D. D. Lee, D. I. Pineda, J. Kriesel, W. A. Hargus, J. W. Bennewitz, B. Bigler, S. A. Danczyk, R. M. Spearrin, Methane-Oxygen Rotating Detonation Exhaust Thermodynamics with Variable Mixing, Equivalence Ratio, and Mass Flux, Aerosp. Sci. Technol. 113 (2021) 106683.

[23] C. Goldenstein, R. Spearrin, J. Jeffries, R. Hanson, Infrared laser-absorption sensing for combustion gases, Prog. Energ. Combust. 60 (2017) 132–176.

[24] L. Rothman, I. Gordon, R. Barber, H. Dothe, R. Gamache, A. Goldman, V. Perevalov, S. Tashkun, J. Tennyson, HITEMP, the High-Temperature Molecular Spectroscopic Database, J. Quant. Spectrosc. Ra. 111 (2010) 2139–2150.

[25] N. Q. Minesi, M. O. Richmond, C. C. Jelloian, N. M. Kuenning, A. P. Nair, R. M. Spearrin, Multi-line Boltzmann regression for near-electronvolt temperature and CO sensing via MHz-rate infrared laser absorption spectroscopy, Appl. Phys. B-Lasers O 128 (2022) 1432–0649.

[26] A. P. Nair, N. Q. Minesi, N. M. Kuenning, A. R. Keller, R. M. Spearrin, Optical pressure sensing at MHz rates via collisional line broadening of carbon monoxide: uncertainty quantification in reacting flows, Appl. Phys. B-Lasers O 129 (2023) 51.

[27] D. D. Lee, F. A. Bendana, R. M. Spearrin, Laser Absorption Spectroscopy of Carbon Monoxide near 4.97 m for Temperature and Species Measurements in Hydrocarbon-Fueled Rockets, in: 2018 AIAA Aerospace Sciences Meeting, 2018, 210059.

[28] D. I. Pineda, F. A. Bendana, K. K. Schwarm, R. M. Spearrin, Multi-isotopologue laser absorption spectroscopy of carbon monoxide for high-temperature chemical kinetic studies of fuel mixtures, Combust. Flame 207 (2019) 379–390.

[29] A. P. Nair, N. Q. Minesi, C. Jelloian, N. M. Kuenning, R. M. Spearrin, Extended tuning of distributed-feedback lasers in a bias-tee circuit via waveform optimization for MHz-rate absorption spectroscopy, Meas. Sci. Technol. 33 (2022) 105104.

[30] A. McLean, C. Mitchell, D. Swanston, Implementation of an efficient analytical approximation to the Voigt function for photoemission lineshape analysis, J. Electron Spectrosc. 69 (1994) 125–132.
[31] R. Hanson, R. Spearrin, C. Goldenstein, Spectroscopy and Optical Diagnostics for Gases, Springer International Publishing, Berlin, Germany, 2016.
[32] I. Gordon, L. Rothman, R. Hargreaves, R. Hashemi, E. Karlovets, F. Skinner, E. Conway, C. Hill, R. Kochanov, Y. Tan, P. Wcisło, A. Finenko, K. Nelson, P. Bernath, M. Birk, V. Boudon, A. Campargue, K. Chance, A. Coustenis, B. Drouin, J. Flaud, R. Gamache, J. Hodges, D. Jacquemart, E. Mlawer, A. Nikitin, V. Perevalov, M. Rotger, J. Tennyson, G. Toon, H. Tran, V. Tyuterev, E. Adkins, A. Baker, A. Barbe, E. Canè, A. Császár, A. Dudaryonok, O. Egorov, A. Fleisher, H. Fleurbaey, A. Foltynowicz, T. Furtenbacher, J. Harrison, J. Hartmann, V. Horneman, X. Huang, T. Karman, J. Karns, S. Kassi, I. Kleiner, V. Kofman, F. Kwabia–Tchana, N. Lavrentieva, T. Lee, D. Long, A. Lukashevskaya, O. Lyulin, V. Makhnev, W. Matt, S. Massie, M. Melosso, S. Mikhailenko, D. Mondelain, H. Müller, O. Naumenko, A. Perrin, O. Polyansky, E. Raddaoui, P. Raston, Z. Reed, M. Rey, C. Richard, R. Tóbiás, I. Sadiek, D. Schwenke, E. Starikova, K. Sung, F. Tamassia, S. Tashkun, J. Vander Auwera, I. Vasilenko, A. Vigasin, G. Villanueva, B. Vispoel, G. Wagner, A. Yachmenev, S. Yurchenko, The HITRAN2020 molecular spectroscopic database, J. Quant. Spectrosc. Ra. 277 (2022) 107949.
[33] R. R. Gamache, B. Vispoel, M. Rey, A. Nikitin, V. Tyuterev, O. Egorov, I. E. Gordon, V. Boudon, Total internal partition sums for the HITRAN2020 database, J. Quant. Spectrosc. Ra. 271 (2021) 107713.
[34] G. P. Smith, D. M. Golden, M. Frenklach, N. W. Moriarty, B. Eiteneer, M. Goldenberg, C. T. Bowman, R. K. Hanson, S. Song, W. C. Gardiner, V. V. Lissianski, Z. Qin, GRI-MECH 3.0 (1999).
URL `http://combustion.berkeley.edu/gri-mech/version30/text30.html`
[35] S. Browne, J. Ziegler, J. E. Shepherd, Numerical Solution Methods for Shock and Detonation Jump Conditions, GALCIT Report FM 2006.006, Graduate Aeronautical Laboratories, California Institute of Technology, CA, USA (2004).
[36] D. G. Goodwin, H. K. Moffat, R. L. Speth, Cantera: An object-oriented software toolkit for chemical kinetics, thermodynamics, and transport processes (2018).
URL `https://cantera.org/`
[37] D. York, N. M. Evensen, M. L. Martinez, J. De Basabe Delgado, Unified equations for the slope, intercept, and standard errors of the best straight line, Am. J. Phys. 72 (2004) 367–375.